Materials Advances

ROYAL SOCIETY OF CHEMISTRY

PAPER

View Article Online
View Journal | View Issue

Check for updates

Cite this: *Mater. Adv.*, 2021, 2, 5752

Performance and limits of 2.0 eV bandgap $CuInGaS_2$ solar absorber integrated with CdS buffer on F:SnO_2 substrate for multijunction photovoltaic and photoelectrochemical water splitting devices†

Nicolas Gaillard, *[a] Wilman Septina,[a] Joel Varley,[b] Tadashi Ogitsu,[b] Kenta K. Ohtaki,[c] Hope A. Ishii,[c] John P. Bradley,[c] Christopher Muzzillo,[d] Kai Zhu,[d] Finn Babbe[e] and Jason Cooper[e]

We report on the electrical properties of 2.0 eV bandgap (E_G) $CuInGaS_2$ (CIGS) solar absorbers integrated on SnO_2:F (FTO) substrates and interfaced with CdS buffer layers for multijunction solar cells and photoelectrochemical water splitting devices. The averaged short-circuit photocurrent density measured on nine ITO/ZnO/CdS/CIGS/FTO cells was 10.0 mA cm^{-2}, a value corresponding to 70% of the optical limit for a 2.0 eV-bandgap absorber. However, the averaged power conversion efficiency was low (avg.: 2.4%) and for the most part limited by modest open circuit voltage values (avg.: 587 mV). Solid-state analyses performed at low temperatures revealed poor energetic alignment at the CdS/CIGS top interface. An activation energy (1.1 eV) for the dominant recombination mechanism significantly lower than the CIGS bandgap was measured, implying that recombination takes place near the CdS/CIGS interface. This finding is supported by the large difference found between the quasi Fermi level splitting of the bare absorber (1.17 eV) and the open circuit voltage of the device. Complementary theoretical calculations identified Fermi level pinning as a possible cause for the poor interface energetics through Cd incorporation on both the Cu and the group-III sites, resulting in a large conduction band offset (~0.9 eV) at the CdS/CIGS interface. This work underlines the need for new E_G-tunable buffers coupled with optimized CIGS surface energetics (*e.g.* ordered vacancy compounds) for future chalcopyrite-based multijunction solar cells and photoelectrochemical water splitting devices.

Received 1st July 2021,
Accepted 18th July 2021

DOI: 10.1039/d1ma00570g

rsc.li/materials-advances

Open Access Article. Published on 19 July 2021. Downloaded on 2/5/2026 4:17:44 PM.
This article is licensed under a Creative Commons Attribution-NonCommercial 3.0 Unported Licence.

1. Introduction

For over four decades, major investments in III–V materials growth and integration have boosted the power conversion efficiency (PCE) of multijunction solar cells (MJSC) to 47.1%,[1] however the costs associated with substrates and processing still relegate this technology to niche applications in the current photovoltaic (PV) market. Although lower cost manufacturing techniques[2,3] and substrates[4] are being developed, it is unclear how long it will take for III–V MJSC to be competitive for utility-scale energy production. Replacing III–Vs entirely with inexpensive material classes could radically change the future of PV, assuming cost savings outweigh efficiency penalties. Amongst all mature PV technologies, bandgap (E_G) tunable, direct absorber, thin film Cu(In,Ga)(S,Se)$_2$ (CIGSSe) chalcopyrites have emerged as potential candidates for low cost/high efficiency MJSC applications. When compared to III–V technologies, chalcopyrites can be processed using economical high-throughput vacuum processing, and recent developments in molecular ink-based techniques[5] could potentially further reduce their manufacturing cost. Also, outstanding PCE has been demonstrated with chalcopyrites, including 23.35% with single junction CIGSe PV[6] and 25.9% with mechanically stacked perovskite/CIGSe tandems.[7]

It is worth noting however that the bandgap tunability of chalcopyrites is not being exploited in most applications, aside from slight bandgap gradings. Narrow-E_G 1.2 eV CIGSe remains

[a] *Hawaii Natural Energy Institute, University of Hawaii, Honolulu, Hawaii 96822, USA. E-mail: ngaillar@hawaii.edu*
[b] *Lawrence Livermore National Laboratory, Livermore, California 94550, USA*
[c] *Hawaii Institute of Geophysics & Planetology, University of Hawaii, Honolulu, Hawaii 96822, USA*
[d] *National Renewable Energy Laboratory, Golden, Colorado 80401, USA*
[e] *Chemical Sciences Division, Lawrence Berkeley National Laboratory, Berkeley, CA 94720, USA*

† Electronic supplementary information (ESI) available. See DOI: 10.1039/d1ma00570g

© 2021 The Author(s). Published by the Royal Society of Chemistry

Open Access Article. Published on 19 July 2021. Downloaded on 2/5/2026 4:17:44 PM.
This article is licensed under a Creative Commons Attribution-NonCommercial 3.0 Unported Licence.

the primary material in all high efficiency chalcopyrite-based technologies, whereas wide-E_G absorbers (*e.g.* 1.67 eV $CuGaSe_2$: CGSe) are still a laboratory curiosity despite their potential for MJSC applications. Research has shown that integrating both narrow and wide-E_G chalcopyrites into monolithic tandems is extremely difficult,[8] since the deposition temperatures required to manufacture the top absorber (>350 °C) would inevitably degrade the heterojunction of the bottom cell.[9] In addition, the vast majority of studies focused on the development of wide-E_G chalcopyrites used reflective molybdenum-coated soda lime glass (SLG) substrates[10–12] making the devices unsuitable for MJSC applications. Attempts to transpose deposition techniques initially developed for Mo-SLG substrates to transparent conductive oxides has exposed some limitations.[13]

In contrast, photoelectrochemical (PEC) water splitting is a field in which chalcopyrites have drawn significant attentions over the past two decades.[14–18] In this application, a photovoltage of at least 1.6 V is required to drive the oxygen and hydrogen evolution reactions, with the solar-to-hydrogen (STH) efficiency being directly proportional to the photocurrent density produced by the device. To date, single junction PEC cells made of metal oxides (*e.g.*, 3.4 eV GaN,[19] 3.7 eV $SrTiO_3$,[20] or 3.2 eV TiO_2,[21]) can only split water with STH efficiency of 1–2% due to their light absorption being restricted to ultraviolet, whereas STH efficiencies as high as 16.2% have been reported with III–V multijunction PEC cells.[22] Although III–V-based PEC cells have shown limited durability in acidic electrolytes,[23] alternatively coupling III–V PV with electrolyzers (PV-E) may prove to be a viable route for long term solar power water splitting,[24,25] assuming again that material costs can be significantly reduced. Regardless, chalcopyrite-based tandems could fill the gap between the low-cost, poor-efficiency single junction metal oxide PEC cells and the high efficiency, yet costly III–V PEC or PV-E tandems. As a PEC cell, chalcopyrites appear to be quite stable under PEC water splitting conditions, with durability exceeding several hundreds of hours in strong acids.[26,27] Also, STH efficiency of 10% has been reported for 1.2 eV CIGSe co-planar PV-E devices,[18] and higher efficiencies can be achieved with chalcopyrite-based tandems,[28] assuming such device can be successfully manufactured.

In this paper, we report on our efforts to integrate wide-E_G chalcopyrite PV on SnO_2:F (FTO) substrates for CIGSSe-based MJSC and PEC water splitting applications. Our recent published results have demonstrated that bandgap tunable $CuGa(S,Se)_2$[29] (CGSSe) and $Cu(In,Ga)S_2$[30] (CIGS) can be successfully integrated on FTO while preventing the formation of resistive SnS_x back interface. With our process, co-evaporated CIGSe precursors are first post-treated with elemental sulfur at 350 °C (dosing stage), and then annealed at 500–550 °C under inert atmosphere (alloying stage). For precursors deposited at temperatures typical for three-stage processes (>500 °C), only Cu-rich films ([Cu]/([In] + [Ga]) > 1) could be sulfurized, yet the sub-bandgap transmission ($\%T_{E<EG}$) of the resulting potassium cyanide (KCN)-etched wide-E_G chalcopyrite was too low ($\%T_{E<EG} < 30\%$), making the absorbers impractical for tandem applications.[29] Our subsequent study demonstrated that Cu-poor CIGSe could be fully sulfurized, but only if the precursors deposition temperature was kept below 350 °C.[30] The resulting 2.0 eV CIGS photocathodes (800 nm thick) exhibited a saturated photocurrent densities (5 mA cm^{-2}) corresponded only to 38% of the optical limit. Further optical analysis revealed that this sub-par performance originated from lower optical absorption prosperities in CIGS compared to baseline wide-E_G chalcopyrite absorbers (*e.g.* CGSe).

This present paper builds upon the results reported in ref. 30 and focuses on the integration of thicker (1200 nm) 2.0 eV CIGS absorbers on FTO and interfaced with CdS buffer layers. After a short overview of CIGS materials microstructural and chemical properties, we present the PV performances of ITO/ZnO/CdS/CIGS/FTO solar cells. The averaged short-circuit photocurrent density (J_{SC}) measured on nine cells was 10 mA cm^{-2} (STH efficiency limit[31] = 12.3%), confirming the potential of 2.0 eV CIGS for efficient PEC water splitting. Also the quasi Fermi level splitting measured on the bare absorber layer (1.17 ± 0.05 eV) showed high potential for the material. However, the average PCE was found to be only 2.4%, and was for the most part hindered by low open circuit voltage (V_{OC}) values that averaged 587 mV. Subsequent solid-state characterization at cryogenic temperatures revealed two important limitations with CIGS absorbers. First, a significant photocurrent suppression was observed at reduced temperatures, a behavior also reported for other sulfur containing chalcogenides (*e.g.*, $Cu_2ZnSn(S,Se)_4$) and typically attributed to an energy barrier at the back contact.[32,33] In contrast, our study shows that the photocurrent suppression in CIGS originates from the absorber itself *via* early freeze-out of the dominant acceptors. More importantly, our experimental data suggest Fermi level pinning (FLP) at the CdS/CIGS interface. Complementary theoretical modeling demonstrates that Cd incorporation in 2.0 eV CIGS sub-surface can account for the FLP, with the particular value sensitive to the deposition and growth conditions and spanning a range of 0.63–1.06 eV depending on how Cu-poor the absorber surface is prior to buffer deposition. Our measurements also exhibited a large (>900 meV) conduction band offset at the CdS/CIGS interface, confirming the need for new buffer materials with energetics that match that of wide-E_G chalcopyrites, such as bandgap tunable $Mg_xZn_{1-x}O$ recently proposed my members of our collaborative team.[34]

2. Methods

Thin film absorbers synthesis

The 2.0 eV 1200 nm-thick Cu-poor CIGS thin film materials used in the present study were obtained by converting 1.4 eV CIGSe precursors co-evaporated on FTO substrates (Hartford Glass, 15 Ω $sq.^{-1}$) with the close-space sulfurization (CSS) process recently reported by our group.[30] In short, FTO substrates were cleaned in an Alconox solution (2 wt%)/DI-water (18 MΩ)/acetone (ACS grade, 99.5%)/DI-water/methanol (ACS grade, 99.5%) sequence each for 10 minutes. The substrates were then dried with compressed nitrogen (pre-purified) and rapidly loaded in a co-evaporation chamber. The CIGSe

Open Access Article. Published on 19 July 2021. Downloaded on 2/5/2026 4:17:44 PM.
This article is licensed under a Creative Commons Attribution-NonCommercial 3.0 Unported Licence.

precursors deposition was carried out at a base pressure of 5 μTorr using a two-stage process comprising a Cu-poor step (stage #1, 150 °C, 8 minutes duration) and a Cu-free growth phase (stage #2, 350 °C, 8 minutes duration). The transition between the Cu-poor stage #1 and Cu-free stage #2 was established by simply turning the Cu source off as soon as the desired Cu thickness, measured by an Electron Impact Emission Spectroscopy monitoring system (EIES, Inficon) instrument, was achieved. Newly formed CIGSe precursors were then placed with elemental sulfur (150 mg) into a cylindrical weighing bottle (Kimble-Chase, borosilicate, 92 mL nominal volume, fritted glass seal) under nitrogen atmosphere in an in-house-built glove-box with O_2 concentration less than or equal to 0.1%. The weighting bottle was then placed into a tube furnace preheated at 350 °C for 60 minutes. The same process was repeated a second time at 500 °C for 10 minutes in absence of sulfur. This two-step dosing-alloying approach led to over 95% substitution of Se with S in CIGSe. Sequencing the sulfurization process permitted to prevent the formation of undesirable resistive SnS_x interfacial layers between the CIGS absorber and the FTO substrate, as demonstrated by TEM/EDX analysis of the back interface. We invite the reader to review ref. 30 for more details about the CSS process.

Solar cells integration

No KCN etching was performed on the absorbers prior to device fabrication. An 80 nm CdS buffer layer was deposited onto the CIGS/FTO samples by chemical bath deposition (CBD). In the CBD process, $CdSO_4$ (0.015 M), NH_4OH (7.2 M), and thiourea (1.5 M) dissolved in deionized water were poured into a water bath previously heated at 85 °C. Samples were then immersed in the solution for 8 min. The CdS-coated CIGS/FTO samples were then annealed in air for 7 min in a laboratory oven (FisherScientific Isotemp 500 Series) set at 120 °C. Finally, the solar cells were completed with RF-sputtered of undoped ZnO (room temperature, 100 nm) and In_2O_3/SnO_2 90/10 wt% (ITO, 200 °C, 500 nm). The total area of each cell (0.12 cm^2) was defined by the diameter of circular holes of the shadow mask used during the ITO deposition. No metallic grids nor anti reflective coatings were used in this experiment.

Solar cells characterization

Indoor current density–voltage (*J–V*) curves of the solar cells were measured at 25 °C using a temperature-controlled stage under simulated $AM1.5_G$ irradiation provided by a 1000 W solar simulator equipped with a Xe bulb and an $AM1.5_G$ filter (Newport, 91192-1000). The solar simulator was calibrated using a spectroradiometer (ITL 900) such that its output power matched that of $AM1.5_G$ in the 250–650 nm range (40.8 mW cm^{-2}). For outdoor testing, the solar cell's temperature (<30 °C) was maintained using a 40 mm fan and *J–V* were measured when the current of an NREL-certified Si photodiode reached its calibrated value for $AM1.5_G$. External quantum efficiency (EQE) was measured with neither electrical nor light biases using a PVMease QEX7 instrument equipped with a 75 W Xe. The monochromatic beam was focused to a 1 mm × 2.5 mm area and chopped at 80 Hz. Temperature-dependent *JV* (*J–V–T*) and capacitance–voltage (*C–V–T*) were measured using a cryostat cooled with liquid-He and equipped with a Lake Shore 335-temperature controller. For *J–V–T*, the devices were illuminated using a white LED lamp which illumination (1 sun) was adjusted until the devices short-circuit current density (J_{SC}) matched that measured with the 1000 W solar simulator. *C–V–T* measurements were performed in dark at 10 kHz and AC voltage of 50 mV using a Biologic SP-200 potentiostat equipped for impedance analysis. The DC bias voltage was swept from 2.5 to −2.5 V, and carrier concentration was extracted using a dielectric constant of 13.6.

Optical, microstructural and elemental analyses

The optical transmittance and reflectance of CIGS integrated on FTO was measured with a UV-visible spectrometer equipped with 100 mm integrating sphere (PerkinElmer, Lambda 750, InGaAs detector). Generated photoluminescence (PL) signals were spectrally resolved in a grating monochromator and detected using a Si detector array (Andor, iDus 420OA). A 405 nm CW laser was used for sample excitation. Microstructural and chemical analyses were carried on an electron transparent thin section of a complete CIGS solar cell prepared using a Helios NanoLab 660 dual-beam focused ion beam instrument (FIB-SEM, FEI/Thermo Fisher) equipped with an X-max N80 SDD-EDX detector (Oxford Instruments). Scanning transmission electron microscope (STEM) images and energy dispersive X-ray spectroscopy (EDX) measurements were collected at 300 kV on a High-base Titan G2 (Scanning) Transmission Electron Microscope (FEI/Thermo Fisher) equipped with a solid-state Si(Li) EDX detector (Genesis 4000, EDAX).

Computational methods

Hybrid functional calculations were performed with the Heyd–Scuseria–Ernzerhof (HSE06) screened hybrid functional and projector-augmented wave (PAW) approach as implemented in the VASP plane-wave code.[35–37] Filled p and d shells of Cu, In, and Ga were treated as core electrons in the PAW potentials. Defect formation energies were evaluated with the formalism as described in ref. 38 using 64-atom supercells for $CuInSe_2$ (CISe), CGSe, $CuInS_2$ (CIS), and $CuGaS_2$ (CGS). The supercell calculations of the bulk chalcopyrites adopted a Hartree–Fock mixing parameter of 32%, a plane-wave energy cutoff of 400 eV, a 2 × 2 × 2 mesh of Monkhorst–Pack special *k*-points and the lattice parameters summarized in ref. 30. Finite-size corrections were incorporated using approach of Freysoldt *et al.*[39] using dielectric constants for the components parallel perpendicular to the chalcopyrite *c*-axis ($\varepsilon_{\parallel}$,$\varepsilon_{\perp}$) for CISe (15.2,16.0), CGSe (12.4,14.4), CIS (10.2,10.2) and CGS (7.6,8.9). The formation energies were evaluated at different chemical potential regimes in the phase diagrams for evaluated using reference phase energies as taken from the Materials Project,[39] with the phase diagrams and reference energies included in the ESI.†

© 2021 The Author(s). Published by the Royal Society of Chemistry

Open Access Article. Published on 19 July 2021. Downloaded on 2/5/2026 4:17:44 PM.
This article is licensed under a Creative Commons Attribution-NonCommercial 3.0 Unported Licence.

3. Results and discussion

Bulk microstructural, chemical and optical properties

The microstructural and chemical properties of 2.0 eV CIGS absorbers synthesized from 1.4 eV CIGSe precursors were reported extensively in our previous communication.[30] Briefly, Raman scattering analyses demonstrated that sulfur incorporation was permitted by poor crystallographic ordering in Cu-poor CIGSe precursors grown at low temperature (350 °C). After sulfurization, 95% of selenium was replaced with sulfur, leading to CIGS absorbers with bandgap energies ranging from 2.0 to 2.45 eV depending on the initial In and Ga content in the precursors. TEM and EDX analyses performed on a 2.0 eV CIGS thin film revealed uniform [Ga]/([Ga] + [In]) (GGI ~ 0.69) and [S]/([S] + [Se]) (SSSe ~ 0.93) distributions in the absorber. New TEM/EDX images of a fully integrated ITO/ZnO/CdS/CIGS/FTO/SLG solar cell used in the present study are presented in Fig. 1. The CIGS absorbers fabricated with the CSS process are made of rather small grains (50–200 nm across) and contain voids, as evidenced by the white regions in the bright field TEM image in Fig. 1(a). This morphology contrasts greatly with that of chalcopyrite absorbers co-evaporated using conventional multi-stage processes, where dense films made of large grains (up to 1 μm across) are usually observed,[12] although in some cases small grain size has been found not to be detrimental to CIGSe solar cells efficiency.[40] Complementary TEM analysis in a zoomed in region of Fig. 1(a) reveals that the dense regions in CIGS are made of highly crystalline grains with clearly defined boundaries, as presented in Fig. 1(b) and (c). The elemental composition of CIGS measured by STEM/EDX point analysis in Fig. S1 (ESI†) is presented in Table S1 (ESI†). The averaged [Cu]/([Ga] + [In]) (CGI), GGI and SSSe measured in the bulk were 0.87, 0.73 and 0.94, respectively. The optical transmittance and reflectance of a CIGS film are presented in Fig. 2(a). An optical bandgap of 2.0 eV, consistent with the GGI of 0.73,[30,41] was estimated. More importantly, optical transmittance as high as 78% on average for photons with energy lower than the bandgap was measured, a value significantly higher than that measured on wide-E_G CGSSe synthesized from Cu-rich CGSe precursors ($\%T_{E<EG} < 30\%$)[29] or CIGS made by sulfurizing Cu/In/Ga metal stacks or alloys ($\%T_{E<EG} < 25\%$).[42]

The potential of an absorber for solar energy conversion can be assessed by the quasi Fermi level splitting (qFLs) using PL measurement at room temperature. In well-optimized narrow bandgap chalcopyrite systems, qFLs and V_{OC} differ typically only by a few 10 meV. The investigated Cu(In,Ga)S_2 absorber has a broad asymmetric PL peak centered around 1.4 eV with a FWHM of 305 meV (Fig. S2, ESI†). This peak is strongly red shifted from the expected bandgap of 2 eV, likely originating from defect to band transitions. Similar red shifted PL has been observed previously also for $CuInS_2$.[43] Since no direct band to band luminescence was observed, Planck's generalized law[44] cannot be applied to extract the qFLs. As a work around, the external radiative efficiency (ERE) was determined using a known reference (see ESI† for more details). A qFLs of (1.17 ± 0.05) eV was calculated using the relationship between the radiative efficiency and the maximum achievable V_{OC} under Schockley–Queisser conditions ($V_{OC,SQ}$) [$V_{OC} = V_{OC,SQ} + k_BT/q \ln(ERE)$].[45] This value corresponds to about 70% of the maximal reachable radiative limit for a 2 eV absorber (1.67 eV)[46] and should thus enable good device performance. Next, PL was measured over two decades of excitation density to extract an optical diode factor[47] of 1.38 (Fig. S2, ESI†). This value is slightly higher than that observed for low bandgap Cu(In,Ga)Se_2 (1.15–1.3),[47] however it should not limit device performance.

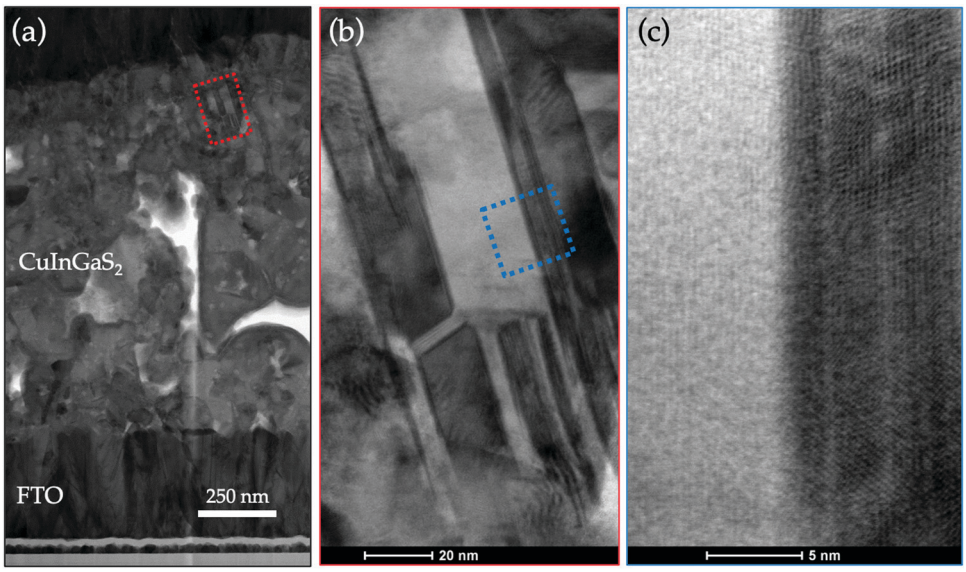

Fig. 1 Bright field STEM micrographs of (a) fully integrated CIGS solar cell and (b) two adjacent CIGS grains located in the box in (a). (c) Zoomed image of the grain boundary in the box in (b) showing high degree of crystallinity.

Open Access Article. Published on 19 July 2021. Downloaded on 2/5/2026 4:17:44 PM.
This article is licensed under a Creative Commons Attribution-NonCommercial 3.0 Unported Licence.

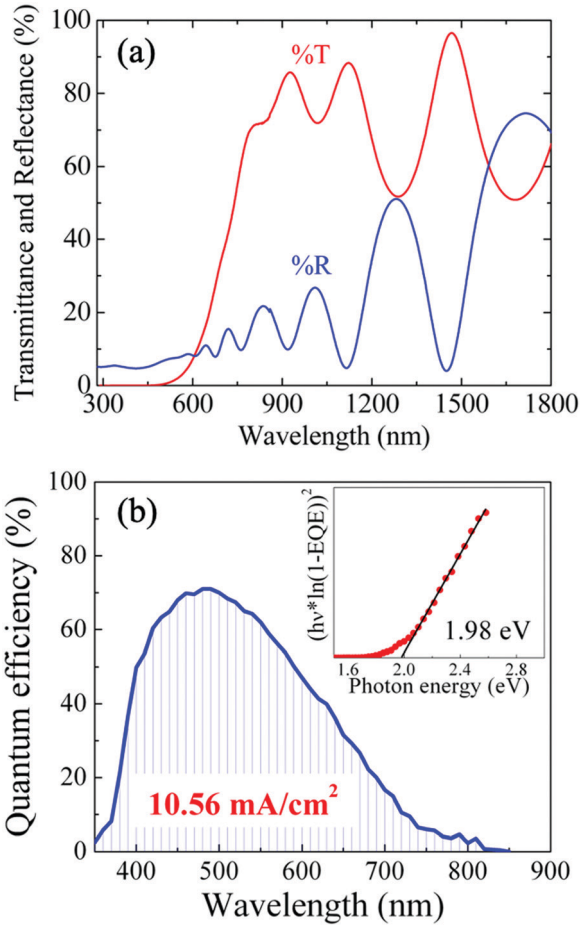

Fig. 2 (a) Optical transmittance and reflectance measured on CIGS integrated on FTO (data corrected for FTO absorption). (b) External quantum efficiency and (inset) $[h\nu \times \ln(1 - \mathrm{EQE})]^2$ *vs.* $h\nu$ curve measured on a 2.0 eV CIGS solar cell.

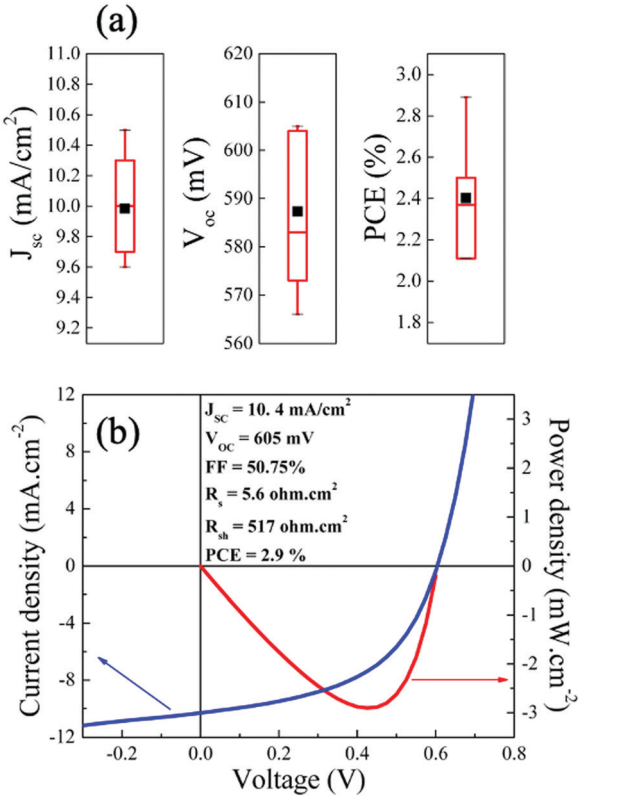

Fig. 3 (a) Statistical distribution of J_{SC}, V_{OC} and PCE measured on nine 2.0 eV CIGS solar cells integrated on 1 FTO substrate. The black squares represent the average value of each parameter. (b) Current *vs.* voltage (blue line) and power *vs.* voltage (red line) characteristics of the champion solar cell.

Solid-state properties of CdS/Cu(In,Ga)S_2/FTO solar cells at room temperature

The EQE of a CIGS solar cell measured under short-circuit conditions is presented in Fig. 2(b). A maximum conversion efficiency of 71% is achieved at 480 nm wavelength. The electronic bandgap, calculated from the $[h\nu \times \ln(1 - \mathrm{EQE})]^2$ *vs.* $h\nu$ curve[48] (Fig. 2(b), inset), was estimated to be ~2.0 eV, consistence with the values measured by optical methods (Fig. 2(a) and Fig. S3, ESI†). Finally, integrating the QE curve over $AM1.5_G$ led to a J_{SC} of 10.56 mA cm^{-2}, representing 70% of the theoretical limit for a 2.0 eV bandgap material (15.1 mA cm^{-2}, assuming the optical limit with no absorption of the ITO/ZnO/CdS stack). Fig. 3(a) presents the statistical distribution of J_{SC}, V_{OC} and PCE measured under simulated $AM1.5_G$ illumination on nine 2.0 eV CIGS solar cells. The current–voltage (J–V) characteristic of the champion solar cell, as determined by PCE (2.9%), is presented in Fig. 3(b), while a comparison of J–V characteristics measured on one representative cell (PCE = 2.4%) under simulated $AM1.5_G$ and outdoor illumination is presented in Fig. S4 (ESI†). All devices yield relatively high J_{SC} (min: 9.6 mA cm^{-2}, max: 10.5 mA cm^{-2}, avg: 10.0 mA cm^{-2}). However, PCE recorded on these solar cells were relatively modest (min: 2.1%, max: 2.9%, avg: 2.4%) and for the most part hindered by low V_{OC} values (min: 566 mV, max: 605 mV avg: 587 mV) considering the absorbers' bandgap. Only about 35% ($V_{OC}/V_{OC,SQ}$)[45] of the maximum achievable V_{OC} are utilized compared to the upper limit of 70% determined from the qFLs of the absorber, indicating a band misalignment at the absorber/buffer interface. In comparison, Merdes *et al.* and Young *et al.* have reported V_{OC} values as high as 879 mV[49] and 910 mV[11] on 1.53 eV CIGS ($V_{OC}/V_{OC,SQ}$ = 70%) and 1.67 eV $CuGaSe_2$ (66%) solar cells, respectively (both integrated on Mo substrates with CdS n-type buffers). Although high-Ga content can limit V_{OC} in chalcopyrite solar cells, the latter usually increases linearly with the bandgap for GGI values up to ~0.3–0.4, and then saturates.[12,49] Following this reasoning, V_{OC} values measured on 2.0 eV CIGS should be at least comparable to, if not higher than, that commonly reported on $CuInS_2$ solar cells (~730 mV).[50]

Solid-state properties of CdS/CIGS/FTO cells at cryogenic temperatures

(i) General overview. To further elucidate the origin of low V_{OC} values measured on wide-E_G CIGS cells at room temperature, complementary solid-state characterizations were gathered at cryogenic temperatures on a representative solar cell (PCE = 2.37%, J_{SC} = 9.7 mA cm^{-2}, V_{OC} = 580 mV, FF = 43.35%) and compared to that of a CIGSe absorber provided by NREL (1.2 eV bandgap, Mo substrate, PCE = 14.8%). The latter was

© 2021 The Author(s). Published by the Royal Society of Chemistry

Open Access Article. Published on 19 July 2021. Downloaded on 2/5/2026 4:17:44 PM.
This article is licensed under a Creative Commons Attribution-NonCommercial 3.0 Unported Licence.

integrated as solar cell using CdS, ZnO and ITO processes identical to those employed in the fabrication of the CIGS solar cell. The *J–V–T* characteristics measured at 150 K, 200 K, 250 K and 300 K on the CIGSe solar cell are presented in Fig. 4(a). Typical behavior reported at low temperatures on efficient chalcopyrite solar cells[51] was observed on the CIGSe device, including temperature-independent J_{SC}, shunt (R_{SH}) and series (R_S) resistances, as well as the increase of V_{OC} with decreasing temperature (see Table S2, ESI† for complete cell characteristics). A notable feature is the early saturation of forward current (roll-over) observed at 150 K. Several models have been proposed to explain such behavior, including the presence of a defect layer either at the absorber sub-surface[52] defects associated with the CdS buffer layer,[53–55] as well as the formation of a Schottky barrier at the CIGSe/Mo back contact interface.[56]

The temperature-dependence of the CIGS solar cell electrical properties differs significantly from that of the CIGSe device (Fig. 4(b), refer to Table S3, ESI† for complete cell characteristics). A clear photocurrent suppression was observed with reduced temperatures, with J_{SC} dropping from 9.37 mA cm^{-2} (300 K) to 4.49 mA cm^{-2} (150 K). Also, V_{OC} was observed first to increase from 300 K (495 mV) to 200 K (640 mV) before decreasing at 150 K (602 mV). Finally, R_S increases significantly as temperature is reduced, from 10.57 Ω cm^2 at 300 K to 41.43 Ω cm^2 at 150 K (Fig. 4(c)). For comparison, R_S values measured on the CIGSe device increased only by 0.2 Ω cm^2 in the same temperature range. We note that R_{SH} measured on the CIGS solar cell were nearly constant between 300 K (202 Ω cm^2) and 150 K (230 Ω cm^2), yet about 5 times lower than those measured on CIGSe.

(ii) Early freeze-out of dominant acceptors in CIGS. To the best of our knowledge, the remarkable difference in temperature-dependence of R_S between selenide-based and sulfur-based chalcopyrite absorbers has not been reported yet. However, similar trends were measured on closely related kesterite materials. Redinger *et al.* measured nearly constant R_S (<1 Ω cm^2, 150–300 K) on pure selenide $Cu_2ZnSnSe_4$ solar cells (0.93 eV), but observed diverging R_S values (2.7 Ω cm^2 at 300 K to 200 Ω cm^2 at 150 K) on sulfo-selenide $Cu_2ZnSn(S,Se)_4$ (CZTSSe) devices (1.23 eV).[32] The authors reported photocurrent suppression, similar to what we observed on the CIGS device. Also, Mitzi *et al.* measured 200 times R_S increase for CZTSSe cells (1.04 eV) from 340 K to 125 K, compared to only 3 times on pure selenide CIGSe ones (1.16 eV).[33] The model commonly used to explain the R_S increase with reduced temperature is the presence of an energetic barrier at the absorber/back contact interface acting as a blocking diode and polarized in a direction opposite to that of the solar cell p–n junction.[57] With the p–n junction under forward bias, the conductivity of the blocking diode (limited by its reverse saturation current) is reduced as the temperature is lowered, which in turns increases the solar cell total series resistance.

The electrical properties of the CIGS/FTO back contact were further investigated to clarify if the blocking diode model applies to this interface. For this analysis, the ITO/ZnO/CdS

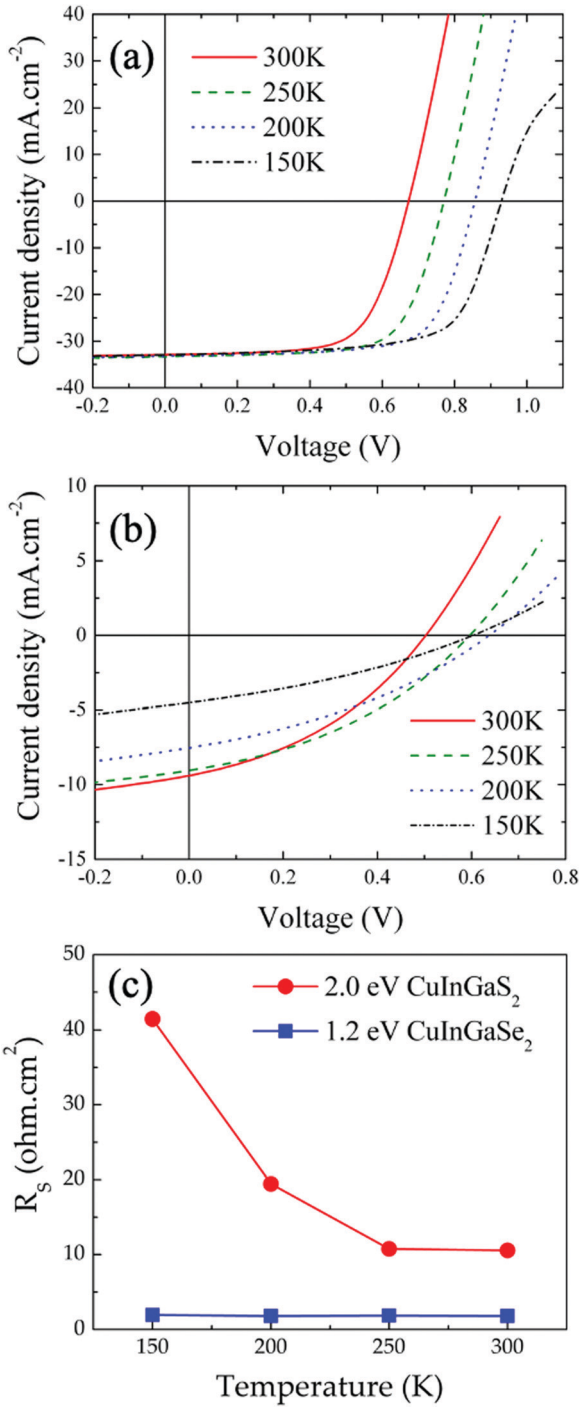

Fig. 4 Temperature dependent current–voltage characteristics measured between 300 K and 150 K on (a) 1.2 eV CIGSe and (b) 2.0 eV CIGS solar cells. (c) Temperature dependence of series resistances measured under AM1.5$_G$ simulated illumination on CIGS (red circles) and CIGSe (blue squares) solar cells.

top layers of the CIGS cell were etched in a 10% HCl solution for 5 minutes and replaced by 100 nm-thick (area: 0.015 cm^2) gold ohmic contacts[58–60] evaporated directly onto the etched CIGS absorber. As presented in Fig. 5(a), all *J–V–T* characteristics measured in dark between 300 K and 140 K on Au/CIGS/FTO are linear and intersects the origin, revealing that an ohmic

Open Access Article. Published on 19 July 2021. Downloaded on 2/5/2026 4:17:44 PM.
This article is licensed under a Creative Commons Attribution-NonCommercial 3.0 Unported Licence.

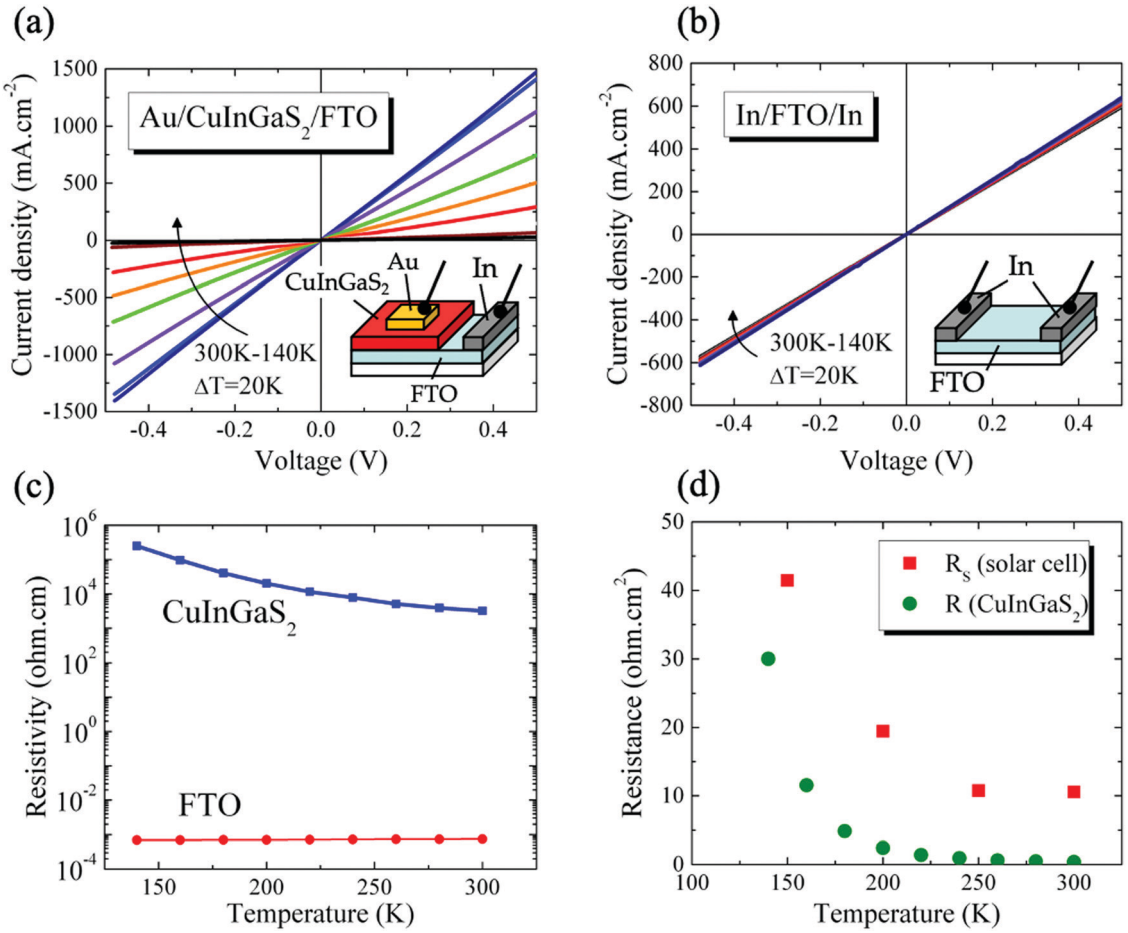

Fig. 5 *J–V* characteristics measured in dark between 300 K and 140 K on (a) Au/CIGS/FTO and (b) In/FTO/In devices. Note that the contact area (*A*) and length (*L*) for each device differ significantly due to their unique geometry. For Au/CIGS/FTO, *A* = pad area = 0.015 cm^2 and *L* = CIGS thickness = 1200 nm. For In/FTO/In, *A* = indium contact width × FTO thickness = 0.8 cm × 400 nm, and *L* = distance between pads = 1.5 cm. (c) Resistivity (Log scale) of CIGS and FTO as function of temperature calculated from *J–V–T* measurements shown in (a and b). (d) Comparison of the temperature dependence of CIGS resistance with that of CIGS solar cell series resistance.

contact, rather than a blocking barrier, is formed at the CIGS/FTO back interface. However, a more rigorous analysis of the CIGS solar cell R_S temperature dependence evidenced a barrier height ϕ_B against hole injection of about 30 meV at the CIGS/FTO interface (Fig. 6). Nonetheless, this value is too low to constitute a blocking barrier and have any significant impact on the cell's electrical properties.[32] Additionally, one can rule out the contribution of the top transparent window layers and buffer, since R_S measured on the CIGSe solar cell integrated with identical CdS, ZnO and ITO layers did not exhibit any temperature dependence (see Fig. 4(c)). Finally, the FTO in-plane resistance was measured in the same temperature range to evaluate its possible contribution to the CIGS solar cell R_S. Here, two indium ohmic contacts (~1 cm^2), distant by ~1.5 cm, were directly soldered onto a clean FTO substrate. As shown in Fig. 5(b), all *J–V–T* curves measured on the In/FTO/In stack exhibit an ohmic behavior and are virtually identical in the 300–140 K range. This demonstrates that the FTO back-contact resistance (as well as that of the In/FTO contacts) does not change with temperature and, as such, cannot be the origin of the CIGS solar cell R_S temperature dependence.

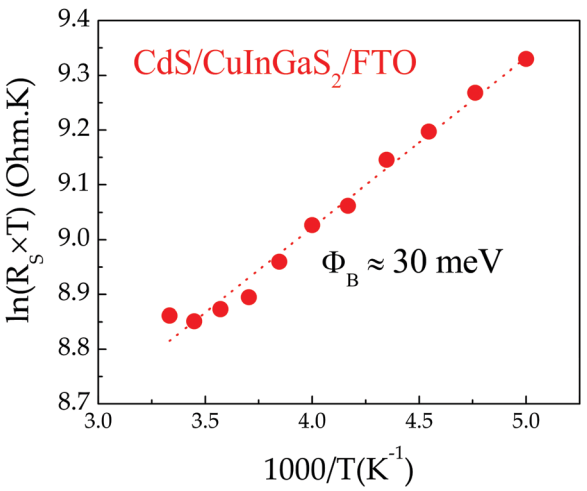

Fig. 6 Arrhenius plot of Ln(R_S × *T*) derived from *J–V–T* measurements performed on CIGS solar cells between 200 K and 300 K. The barrier height ϕ_B at the CIGS/FTO interface is determined by fitting the plot to $R_S = (k/qA \times T)\exp(\phi_B/kT)$, with *A* the effective Richardson constant.

© 2021 The Author(s). Published by the Royal Society of Chemistry

Open Access Article. Published on 19 July 2021. Downloaded on 2/5/2026 4:17:44 PM.
This article is licensed under a Creative Commons Attribution-NonCommercial 3.0 Unported Licence.

We conclude that the change in R_S measured on the CIGS solar cell originates from the absorber itself. Fig. 5(c) presents the temperature-dependence of CIGS resistivity calculated using the *J–V–T* data measured on Au/CIGS/FTO (Fig. 5(a)). The absorber's resistivity increases by nearly two orders of magnitude between 300 K (3.2×10^3 Ω cm) and 140 K (250×10^3 Ω cm). Comparatively, the resistivity of FTO, calculated from the *J–V–T* measured on the In/FTO/In stack (Fig. 5(c)), remained unchanged (7.4×10^{-4} Ω cm at 300 K; 6.9×10^{-4} Ω cm at 140 K). Also, we compare in Fig. 5(d) the temperature-dependence of R_S to that of the CIGS resistance (calculated directly form the *J–V–T* data presented in Fig. 5(c)). The influence of the bulk resistance on the R_S is clearly observed, with R_S increase coinciding with that of CIGS resistance at temperatures below 250 K. Above this temperature, the contribution of CIGS is negligible and the solar cell R_S is dominated by resistances outside of the junction (10.57 Ω cm^2). These results suggest a carrier freeze-out mechanism with reducing temperature from larger ionization of the dominant acceptors in the absorber,[61] as evidenced by the depth profiles of apparent doping density measured as function of temperature (75–300 K) and presented in Fig. S5 (ESI†). Unlike CIGSe, for which a constant N_{CV} measured at 0 V was observed throughout the entire temperature range ($\sim 5 \times 10^{15}$ cm^{-3}, Table S4, ESI†), a two-order of magnitude reduction in doping density was measured in CIGS ($\sim 3 \times 10^{17}$ cm^{-3} to $\sim 3 \times 10^{15}$ cm^{-3}, Table S4, ESI†). Other temperature-dependent contributions from non-ohmic barriers may be also present, such as between grains in the absorber layer[57] or at the absorber-buffer interface as presented in the next section.

(iii) Evidence of Fermi level pinning at the CdS/CIGS interface. The V_{OC} temperature-dependence of both CIGS and CIGSe solar cells were further analyzed to determine the dominant recombination path in each structure. As showed in Fig. 7(a), the activation energy E_A (1.14 eV) of the dominant recombination process in CIGSe, as defined by the linear extrapolation of $V_{OC}(T)$ to 0 K,[62] equates the absorber E_G (1.2 eV), revealing that Shockley–Read–Hall recombination dominates in the absorber bulk. However, the same analysis performed on the CIGS cell and presented in Fig. 7(b) evidenced an activation energy (1.10 eV) significantly lower than the absorber bandgap, suggesting dominant recombination at the absorber/buffer interface. Analogous E_A trends between narrow-E_G selenide- and wide-E_G sulfide-based chalcopyrites were also reported by Thompson *et al.*, with $E_A \approx E_G$ for 1.18 eV CIGSe (E_A = 1.21 eV) and 1.41 eV CIGSe (E_A = 1.42 eV), but $E_A < E_G$ for 1.53 eV $CuInS_2$ (E_A = 1.10 eV), with all solar cells integrated with CdS buffer layers.[63] Shukla *et al.* also reported an activation energy (1.47 eV) significantly lower than the CIGS absorber bandgap (1.7 eV).[64] The large disparity between E_G and E_A can occur due to a defective interface and/or non-ideal alignment of energy bands at the CdS/CIGS heterojunction (a "cliff-like" conduction band offset, CBO). Another fundamental difference observed between the CIGSe and CIGS solar cells is the saturation open circuit voltage (V_{SAT}), a parameter representing the maximum quasi-Fermi level split (QFLS) achievable before freeze-out of the recombination mechanism dominating at room temperature. For CIGSe, V_{SAT} is achieved at 90 K, with a value (990 mV) corresponding roughly to 75% of E_G/q. In contrast, V_{SAT} measured on CIGS (636 mV) represents only 33% of E_G/q and is achieved at a much higher temperature (200 K), suggesting possible pinning of the Fermi level (FLP) at the heterointerface.[65] Shukla *et al.* reported a V_{SAT} at the same temperature on 1.7 eV CIGS solar cells co-evaporated on Mo, although their value (approx. 1 V) corresponded to 58% of E_G/q.

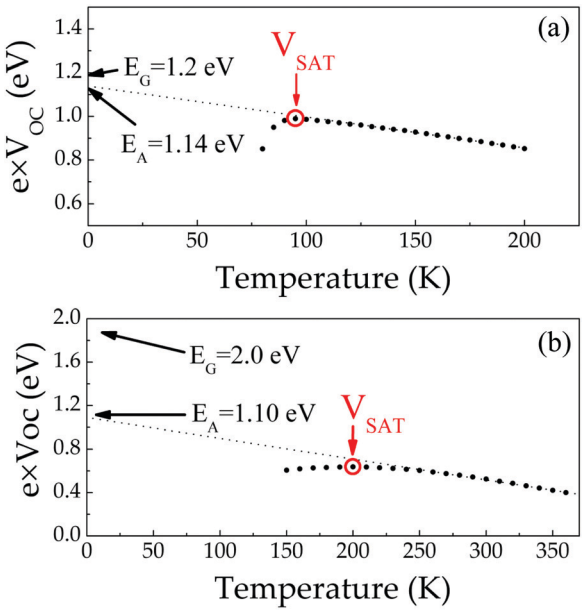

Fig. 7 Temperature dependent open circuit voltage measured between 300 K and 150 K on (a) 1.2 eV CIGSe and (b) 2.0 eV CIGS solar cells.

Theoretical calculations were conducted to further understand the origin of this apparent FLP at the junction between CIGS and CdS. We first consider the influence of possible degradation of the CdS/CIGS interface in Fig. 8 through interfacial impurities, which summarizes the formation energies of incorporated Cd defects calculated in the parent compounds of $CuInS_2$ and $CuGaS_2$ in the Cu-poor growth conditions (Fig. 8(a)) most relevant to the synthesized 2.0 eV CIGS absorbers. For both $CuInS_2$ and $CuGaS_2$, we find that Cd may favorably incorporate on both the Cu site, acting as a shallow donor, and the group-III site, acting as an acceptor. Cadmium interstitials are predicted to be significantly higher in energy. Thus at the interface, Cd incorporation would be expected to lead to self-compensation that would pin the interfacial Fermi level near where the Cd_{Cu} and Cd_{In} concentrations are equivalent, assuming their concentration exceeds that of electrically-active native defects. This pinning level is shown as the dashed lines in Fig. 8(b and c), which we find to occur between $\sim$0.3–0.75 eV above the valence band maximum in $CuInS_2$, and $\sim$0.75–1.2 eV in $CuGaS_2$, for conditions spanning more S-rich/III-poor to S-poor/III-rich limits. Approximating this Fermi level window in the 2.0 eV band gap CIGS absorber from the 0.73 GGI-weighted average, this would suggest the interfacial Fermi level would be pinned within a window of 0.63–1.06 eV for Cu-poor

Open Access Article. Published on 19 July 2021. Downloaded on 2/5/2026 4:17:44 PM.
This article is licensed under a Creative Commons Attribution-NonCommercial 3.0 Unported Licence.

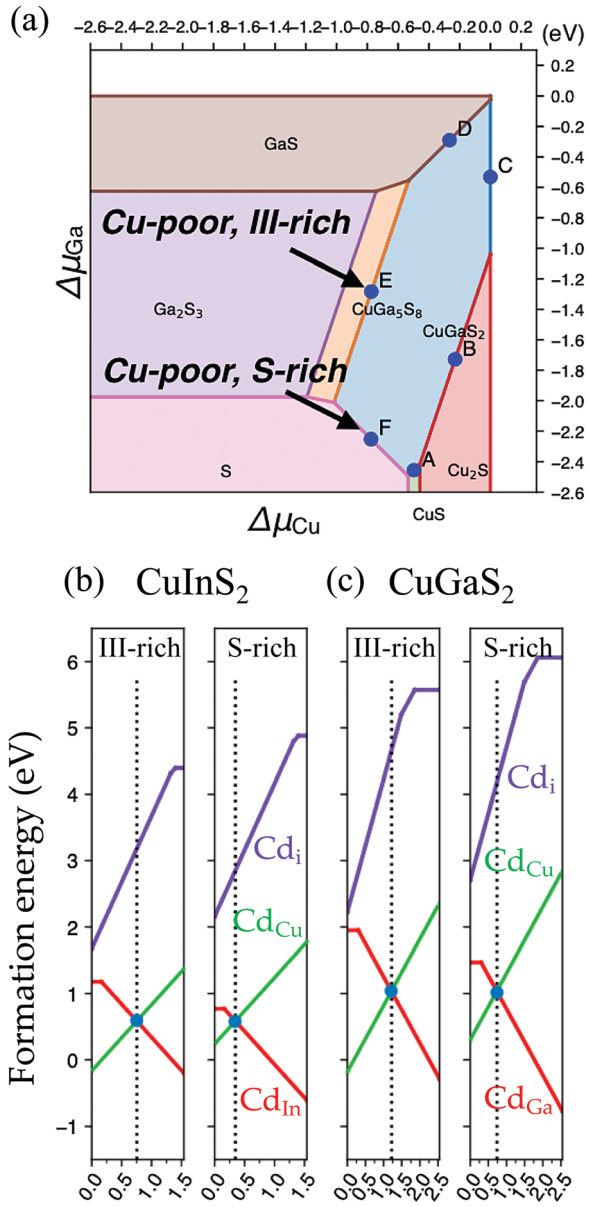

Fig. 8 (a) Representative chalcopyrite phase diagram, calculated for $CuGaS_2$ and shown as a function of the Ga and Cu chemical potentials (μ). The calculated formation energies of dilute Cd impurities are included for $CuInS_2$ (b) and $CuGaS_2$ (c), shown for conditions representing the regimes of Cu-poor and III-rich/S-poor and S-rich/III-poor limits, as also highlighted in (a). The Fermi level that would result from self-compensation from Cd incorporation is included as the dashed lines in (b and c).

conditions spanning the S-rich/III-poor to S-poor/III-rich limits. The entire range of interfacial Fermi-levels achievable is substantially lower than the band gap, with the lowest values predicted in the more Cu- and III-poor limit most consistent with the measured V_{SAT} (636 meV). This suggests a severe detrimental impact to the achievable V_{OC} with interfacial Cd incorporation in the sulfide absorbers.

We also note that this same analysis performed for the CIGSe absorbers suggests an analogous pinning level of 0.56–0.90 eV for the Cu-poor and Se-rich/III-poor to Se-poor/III-rich limits that is essentially independent of the GGI (see Fig. S6 and Table S5, ESI†). This window of Fermi levels falls much closer to the band gaps and the measured V_{SAT} (990 mV) in low-gap CIGSe absorbers supports the observation that the achievable V_{OC} in CIGSe is robust to substantial interfacial Cd incorporation beyond the typical picture of Cd_{Cu} donors incorporated onto vacant Cu sites during CdS deposition.

The nature of CBO at the buffer/absorber interface also plays a critical role in the device performance. Unlike CdS/CIGSe interfaces, for which small "spike-like"[66] (<50 meV) or nearly flat[67] CBO are generally observed, the "cliff-like"[68] CBO brings E_C in CdS closer to E_V in CIGS and facilitates interface recombination. From calculated natural band alignments in ref. 69 and the analysis of the CIGS band edges with composition,[30] we estimate a cliff-like CBO of ~0.5–0.6 eV for 0.73 GGI CdS/CIGS heterojunction. If we also consider the possible formation of off-stoichiometric Cu-deficient phases, or ordered vacancy compounds (OVCs) in the sulfide interface, this can also influence the resulting band offsets with CdS. The OVC compounds tend to slightly increase the band gaps relative to the parent CIGSSe chalcopyrite phases in conjunction with an overall lowering of the band edge positions on an absolute energy scale, thus diminishing the expected cliff with CdS.[70] Taking a GGI-weighted value for the CBO of the $CuIn_5S_8$ relative to $CuInS_2$ (−0.42 eV) and $CuGa_5S_8$ relative to $CuGaS_2$ (−0.79 eV),[70] we obtain an estimated cliff-like CBO of −0.68 eV for a possible OVC alloy relative to the parent CIGS alloy. Taken with the CdS band edge positions, this would suggest the OVC formation would favorably improve the band alignment in the sulfide absorbers, leading to a significantly reduced cliff-like CBO of ~0.1–0.2 eV. While this estimate assumes full miscibility in the OVC and no bowing effects, it gives a reasonable quantitative approximation for how these deficient phases would impact the overall band diagram of the device. Most importantly, it suggests that any OVCs, if present, would be beneficial from the standpoint of improving the band alignment of the sulfide absorber with the CdS buffer layer. With the current OVC-free CdS/CIGS interface, we estimate a CBO ($\sim E_G$–E_A)[71] of approx. 0.9 eV (Fig. 9), a value larger than the

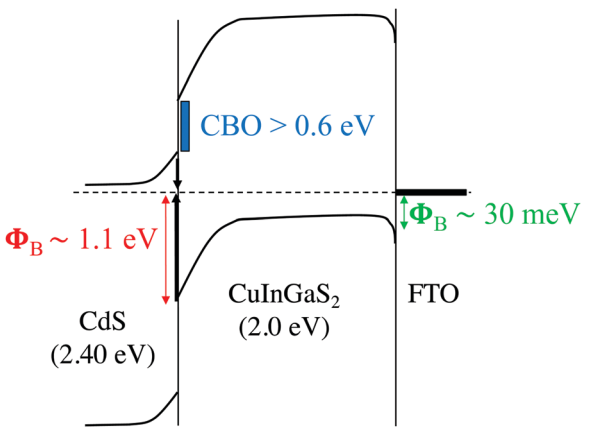

Fig. 9 Tentative band diagram of the CdS/CIGS/FTO structure derived from solid-state measurements at cryogenic temperatures (not to scale).

© 2021 The Author(s). Published by the Royal Society of Chemistry

Open Access Article. Published on 19 July 2021. Downloaded on 2/5/2026 4:17:44 PM.
This article is licensed under a Creative Commons Attribution-NonCommercial 3.0 Unported Licence.

~0.6 eV determined from the theoretical natural band offsets that neglect potentially important interfacial details such as strain and local atomic structure. Nonetheless, the results support the poor conduction band alignment of CdS with 2.0 eV CIGS and emphasize the need for OVCs or E_G-tunable buffers, such as $Mg_xZn_{1-x}O$[34] or Zn(O,S),[72] to reduce interfacial CBO.

4. Conclusions

We have reported on the solid-state properties of 2.0 eV CIGS solar absorbers integrated on FTO substrates and interfaced with CdS buffer layers. In contrast with methods commonly reported for the synthesis of CIGS (sulfurization of Cu-rich metal stacks), our protocol permitted the fabrication of thin film absorbers with high optical transmittance for photons with energy lower than the bandgap ($\%T_{E<EG}$ = 78%), an important attribute for tandem PV and PEC applications. The averaged short-circuit photocurrent density measured on 9 cells was 10.0 mA cm^{-2}, a value corresponding to 70% of the optical limit for a 2.0 eV bandgap absorber. Also the quasi Fermi level splitting of 1.17 eV measured on the bare absorber corresponds to 70% of the maximal achievable value. However, PCE recorded were low (avg.: 2.4%) and, for the most part, hindered by modest V_{OC} values (avg.: 587 mV). Subsequent analyses performed at low temperatures revealed significant photocurrent suppression, a behavior typically attributed to an energy barrier at the back contact. In the case of CIGS, we demonstrate that the photocurrent suppression originates from the absorber itself *via* early freeze-out of the dominant acceptors. Theoretical calculations suggest that Cd may favorably incorporate on both the Cu site, acting as a shallow donor, and the group-III site, acting an acceptor, leading to self-compensation that would pin the interfacial Fermi level. The resulting conduction band offset (~0.9 eV) was found to be much higher than that typically reported for high efficiency devices (~0–0.1 eV). Both FLP and the poor conduction band alignment of CdS with 2.0 eV CIGS emphasize the need for new OVCs or E_G-tunable buffers in future chalcopyrite-based MJSC.

Conflicts of interest

There are no conflicts to declare.

Acknowledgements

This work was funded by the U.S. Department of Energy under contract DE-EE0008085. This work was authored in part by the National Renewable Energy Laboratory, operated by Alliance for Sustainable Energy, LLC, for the U.S. Department of Energy (DOE) under Contract No. DE-AC36-08GO28308. Funding provided by the U.S. Department of Energy, Office of Energy Efficiency and Renewable Energy, Hydrogen and Fuel Cell Technology Office. The views expressed in the article do not necessarily represent the views of the DOE or the U.S. Government. The U.S. Government retains and the publisher, by accepting the article for publication, acknowledges that the U.S. Government retains a nonexclusive, paid-up, irrevocable, worldwide license to publish or reproduce the published form of this work, or allow others to do so, for U.S. Government purposes.

References

1 J. F. Geisz, R. M. France, K. L. Schulte, M. A. Steiner, A. G. Norman, H. L. Guthrey, M. R. Young, T. Song and T. Moriarty, *Nat. Energy*, 2020, **5**, 326–335.
2 J. Chen and C. E. Packard, *Sol. Energy Mater. Sol. Cells*, 2021, **225**, 111018.
3 F. Dimroth, M. Grave, P. Beutel, U. Fiedeler, C. Karcher, T. N. D. Tibbits, E. Oliva, G. Siefer, M. Schachtner, A. Wekkeli, A. W. Bett, R. Krause, M. Piccin, N. Blanc, C. Drazek, E. Guiot, B. Ghyselen, T. Salvetat, A. Tauzin, T. Signamarcheix, A. Dobrich, T. Hannappel and K. Schwarzburg, *Prog. Photovoltaics*, 2014, **22**, 277–282.
4 S. Fan, Z. J. Yu, R. D. Hool, P. Dhingra, W. Weigand, M. Kim, E. D. Ratta, B. D. Li, Y. Sun, Z. C. Holman and M. L. Lee, *Cell Rep. Phys. Sci.*, 2020, **1**, 100208.
5 W. Septina, C. P. Muzzillo, C. L. Perkins, A. C. Giovanelli, T. West, K. K. Ohtaki, H. A. Ishii, J. P. Bradley, K. Zhu and N. Gaillard, *J. Mater. Chem. A*, 2021, **9**, 10419–10426.
6 M. Nakamura, K. Yamaguchi, Y. Kimoto, Y. Yasaki, T. Kato and H. Sugimoto, *IEEE*, 2019, **9**, 1863–1867.
7 D. H. Kim, C. P. Muzzillo, J. Tong, A. F. Palmstrom, B. W. Larson, C. Choi, S. P. Harvey, S. Glynn, J. B. Whitaker, F. Zhang, Z. Li, H. Lu, M. F. A. M. van Hest, J. J. Berry, L. M. Mansfield, Y. Huang, Y. Yan and K. Zhu, *Joule*, 2019, **3**, 1734–1745.
8 J. H. Wi, W. S. Han, W. J. Lee, D. H. Cho, H. J. Yu, C. W. Kim, C. Jeong, J. H. Yun, C.-I. Il Kim and Y. D. Chung, *IEEE J. Photovoltaics*, 2018, **8**, 840–848.
9 S. Kijima and T. Nakada, *Appl. Phys. Express*, 2008, **1**, 0750021.
10 F. Larsson, N. S. Nilsson, J. Keller, C. Frisk, V. Kosyak, M. Edoff and T. Törndahl, *Prog. Photovoltaics*, 2017, **25**, 755–763.
11 D. L. Young, J. Keane, A. Duda, J. A. M. AbuShama, C. L. Perkins, M. Romero and R. Noufi, *Prog. Photovoltaics*, 2003, **11**, 535–541.
12 M. A. Contreras, L. M. Mansfield, B. Egaas, J. Li, M. Romero, R. Noufi, E. Rudiger-Voigt and W. Mannstadt, *2011 37th IEEE Photovoltaic Specialists Conference, IEEE*, 2011, vol. 1, pp. 000026–000031.
13 T. Nakada, Y. Hirabayashi, T. Tokado, D. Ohmori and T. Mise, *Sol. Energy*, 2004, **77**, 739–747.
14 B. Marsen, B. Cole and E. L. Miller, *Sol. Energy Mater. Sol. Cells*, 2008, **92**, 1054–1058.
15 N. Gaillard, D. Prasher, J. Kaneshiro, S. Mallory and M. Chong, *Mater. Res. Soc. Symp. Proc.*, 2013, **1558**, mrss13-1558-z02-07.

© 2021 The Author(s). Published by the Royal Society of Chemistry

Open Access Article. Published on 19 July 2021. Downloaded on 2/5/2026 4:17:44 PM.
This article is licensed under a Creative Commons Attribution-NonCommercial 3.0 Unported Licence.

16 J. Kim, T. Minegishi, J. Kobota and K. Domen, *Energy Environ. Sci.*, 2012, **5**, 6368–6374.
17 D. Yokoyama, T. Minegishi, K. Maeda, M. Katayama, J. Kubota, A. Yamada, M. Konagai and K. Domen, *Electrochem. Commun.*, 2010, **12**, 851–853.
18 T. J. Jacobsson, V. Fjällström, M. Sahlberg, M. Edoff and T. Edvinsson, *Energy Environ. Sci.*, 2013, **6**, 3676.
19 M. G. Kibria, F. A. Chowdhury, S. Zhao, B. AlOtaibi, M. L. Trudeau, H. Guo and Z. Mi, *Nat. Commun.*, 2015, **6**, 1–8.
20 Y. Goto, T. Hisatomi, Q. Wang, T. Higashi, K. Ishikiriyama, T. Maeda, Y. Sakata, S. Okunaka, H. Tokudome, M. Katayama, S. Akiyama, H. Nishiyama, Y. Inoue, T. Takewaki, T. Setoyama, T. Minegishi, T. Takata, T. Yamada and K. Domen, *Joule*, 2018, **2**, 509–520.
21 A. Fujishima and K. Honda, *Nature*, 1972, **238**, 37–38.
22 J. L. Young, M. A. Steiner, H. Döscher, R. M. France, J. A. Turner and T. G. Deutsch, *Nat. Energy*, 2017, **2**, 17028.
23 P. Varadhan, H. C. Fu, Y. C. Kao, R. H. Horng and J. H. He, *Nat. Commun.*, 2019, **10**, 1–9.
24 A. Nakamura, Y. Ota, K. Koike, Y. Hidaka, K. Nishioka, M. Sugiyama and K. Fujii, *Appl. Phys. Express*, 2015, **8**, 107101.
25 J. Jia, L. C. Seitz, J. D. Benck, Y. Huo, Y. Chen, J. W. D. Ng, T. Bilir, J. S. Harris and T. F. Jaramillo, *Nat. Commun.*, 2016, **7**, 1–6.
26 C. P. Muzzillo, W. E. Klein, Z. Li, A. D. Deangelis, K. Horsley, K. Zhu and N. Gaillard, *ACS Appl. Mater. Interfaces*, 2018, **10**, 19573–19579.
27 M. Moriya, T. Minegishi, H. Kumagai, M. Katayama, J. Kubota and K. Domen, *J. Am. Chem. Soc.*, 2013, **135**, 3733–3735.
28 L. C. Seitz, Z. Chen, A. J. Forman, B. A. Pinaud, J. D. Benck and T. F. Jaramillo, *ChemSusChem*, 2014, **7**, 1372–1385.
29 A. D. Deangelis, K. Horsley and N. Gaillard, *J. Phys. Chem. C*, 2018, **122**, 14304–14312.
30 N. Gaillard, D. Prasher, M. Chong, A. Deangelis, K. Horsley, H. A. Ishii, J. P. Bradley, J. Varley and T. Ogitsu, *ACS Appl. Energy Mater.*, 2019, **2**, 5515–5524.
31 N. Gaillard and A. Deangelis, in *Solar to Chemical Energy Conversion: Theory and Application*, ed. M. Sugiyama, K. Fujii and S. Nakamura, Springer International Publishing, Cham, 2016, pp. 261–279.
32 A. Redinger, M. Mousel, M. H. Wolter, N. Valle and S. Siebentritt, *Thin Solid Films*, 2013, vol. 535, pp. 291–295.
33 D. B. Mitzi, O. Gunawan, T. K. Todorov and D. A. R. Barkhouse, *Philos. Trans. R. Soc., A*, 2013, **371**, 20110432.
34 I. S. Khan, C. P. Muzzillo, C. L. Perkins, A. G. Norman, J. L. Young, N. Gaillard and A. Zakutayev, *J. Phys. Energy*, 2021, **3**, 024001.
35 J. Heyd, G. E. Scuseria and M. Ernzerhof, *J. Chem. Phys.*, 2003, **118**, 8207–8215.
36 G. Kresse and J. Furthmüller, *Phys. Rev. B: Condens. Matter Mater. Phys.*, 1996, **54**, 11169–11186.
37 G. Kresse and J. Furthmüller, *Comput. Mater. Sci.*, 1996, **6**, 15–50.
38 C. Freysoldt, B. Grabowski, T. Hickel, J. Neugebauer, G. Kresse, A. Janotti and C. G. Van de Walle, *Rev. Mod. Phys.*, 2014, **86**, 253–305.
39 C. Freysoldt, J. Neugebauer and C. G. Van de Walle, *Phys. Rev. Lett.*, 2009, **102**, 16402.
40 P. Jackson, R. Würz, U. Rau, J. Mattheis, M. Kurth, T. Schlötzer, G. Bilger and J. H. Werner, *Prog. Photovoltaics*, 2007, **15**, 507–519.
41 M. Bär, W. Bohne, J. Röhrich, E. Strub, S. Lindner, M. C. Lux-Steiner, C.-H. Fischer, T. P. Niesen and F. Karg, *J. Appl. Phys.*, 2004, **96**, 3857–3860.
42 N. Gaillard, *Wide Band Gap Chalcopyrite Photoelectrodes for Direct Water Splitting - Final report to the U.S. Department of Energy (EE0006670)*, Golden, CO (United States), 2019.
43 A. Lomuscio, T. Rödel, T. Schwarz, B. Gault, M. Melchiorre, D. Raabe and S. Siebentritt, *Phys. Rev. Appl.*, 2019, **11**, 1.
44 P. Wurfel, *J. Phys. C: Solid State Phys.*, 1982, **15**, 3967–3985.
45 T. Kirchartz and U. Rau, *Adv. Energy Mater.*, 2018, **8**, 1703385.
46 A. Polman, M. Knight, E. C. Garnett, B. Ehrler and W. C. Sinke, *Science*, 2016, **352**, aad4424.
47 F. Babbe, L. Choubrac and S. Siebentritt, *Sol. RRL*, 2018, **2**, pp. 1–6.
48 D. B. Mitzi, O. Gunawan, T. K. Todorov, K. Wang and S. Guha, *Sol. Energy Mater. Sol. Cells*, 2011, **95**, 1421–1436.
49 S. Merdes, R. Mainz, J. Klaer, A. Meeder, H. Rodriguez-Alvarez, H. W. Schock, M. C. Lux-Steiner and R. Klenk, *Sol. Energy Mater. Sol. Cells*, 2011, **95**, 864–869.
50 R. Klenk, J. Klaer, R. Scheer, M. C. Lux-Steiner, I. Luck, N. Meyer and U. Rühle, *Thin Solid Films*, 2005, **480–481**, 509–514.
51 Q. Cao, O. Gunawan, M. Copel, K. B. Reuter, S. J. Chey, V. R. Deline and D. B. Mitzi, *Adv. Energy Mater.*, 2011, **1**, 845–853.
52 A. O. Pudov, A. Kanevce, H. A. Al-Thani, J. R. Sites and F. S. Hasoon, *J. Appl. Phys.*, 2005, **97**, 064901.
53 M. Burgelman, F. Engelhardt, J. F. Guillemoles, R. Herberholz, M. Igalson, R. Klenk, M. Lampert, T. Meyer, V. Nadenau, A. Niemegeers, J. Parisi, U. Rau, H.-W. Schock, M. Schmitt, O. Seifert, T. Walter and S. Zott, *Prog. Photovoltaics*, 1997, **5**, 121–130.
54 J. B. Varley and V. Lordi, *J. Appl. Phys.*, 2014, **116**, 63505.
55 J. B. Varley, V. Lordi, X. He and A. Rockett, *J. Appl. Phys.*, 2016, **119**, 25703.
56 T. Eisenbarth, T. Unold, R. Caballero, C. A. Kaufmann and H.-W. Schock, *J. Appl. Phys.*, 2010, **107**, 034509.
57 O. Gunawan, T. K. Todorov and D. B. Mitzi, *Appl. Phys. Lett.*, 2010, **97**, 233506.
58 P. J. Rostan, J. Mattheis, G. Bilger, U. Rau and J. H. Werner, *Thin Solid Films*, 2005, **480–481**, 67–70.
59 N. Neugebohrn, M. S. Hammer, J. Neerken, J. Parisi and I. Riedel, *Thin Solid Films*, 2015, **582**, 332–335.
60 T. Nakada, Y. Hirabayashi and T. Tokado, *Jpn. J. Appl. Phys.*, 2002, **41**, L1209–L1211.
61 O. Gunawan, T. K. Todorov and D. B. Mitzi, *Appl. Phys. Lett.*, 2010, **97**, 233506.

© 2021 The Author(s). Published by the Royal Society of Chemistry

Open Access Article. Published on 19 July 2021. Downloaded on 2/5/2026 4:17:44 PM.
This article is licensed under a Creative Commons Attribution-NonCommercial 3.0 Unported Licence.

62 V. Nadenau, U. Rau, A. Jasenek and H. Schock, *J. Appl. Phys.*, 2000, **87**, 584.
63 C. P. Thompson, S. Hegedus, W. Shafarman and D. Desai, *33rd IEEE Photovolt. Spec. Conf.*, 2008, 1–6.
64 S. Shukla, D. Adeleye, M. Sood, F. Ehre, A. Lomuscio, T. P. Weiss, D. Siopa, M. Melchiorre and S. Siebentritt, *Phys. Rev. Mater.*, 2021, **5**, 055403.
65 J. D. Cohen, *Identifying the Electronic Properties Relevant to Improving the Performance of High Band-Gap Copper Based I-III-VI2 Chalcopyrite Thin Film Photovoltaic Devices: Final Subcontract Report -NREL/SR-520-43909*, 2007.
66 D. Hauschild, D. Kreikemeyer-Lorenzo, P. Jackson, T. M. Friedlmeier, D. Hariskos, F. Reinert, M. Powalla, C. Heske and L. Weinhardt, *ACS Energy Lett.*, 2017, **2**, 2383–2387.
67 M. Morkel, L. Weinhardt, B. Lohmüller, C. Heske, E. Umbach, W. Riedl, S. Zweigart and F. Karg, *Appl. Phys. Lett.*, 2001, **79**, 4482–4484.
68 L. Weinhardt, O. Fuchs, D. Groß, G. Storch, E. Umbach, N. G. Dhere, A. A. Kadam, S. S. Kulkarni and C. Heske, *Appl. Phys. Lett.*, 2005, **86**, 1–3.
69 J. B. Varley, V. Lordi, T. Ogitsu, A. Deangelis, K. Horsley and N. Gaillard, *J. Appl. Phys.*, 2018, **123**, 161408.
70 A. Sharan, F. P. Sabino, A. Janotti, N. Gaillard, T. Ogitsu and J. B. Varley, *J. Appl. Phys.*, 2020, **127**, 065303.
71 M. Turcu, O. Pakma and U. Rau, *Appl. Phys. Lett.*, 2002, **80**, 2598–2600.
72 S. Shukla, M. Sood, D. Adeleye, S. Peedle, G. Kusch, D. Dahliah, M. Melchiorre, G.-M. Rignanese, G. Hautier, R. Oliver and S. Siebentritt, *Joule*, 2021, **5**, 1816–1831.